Prospects of spatial resolution in vibrational electron energy loss spectroscopy: Implications of dipolar scattering

Christian Dwyer*
Department of Physics, Arizona State University, Tempe, Arizona 85287, USA
(Received 30 September 2017; published 11 December 2017)

We use scattering theory to study the spatial resolution achievable in vibrational energy loss spectroscopy using a focused beam of high-energy (∼100 keV) electrons. We first outline a theory for calculating vibrational-spectroscopic images of crystalline or noncrystalline materials at nanometer spatial resolution or better (up to atomic resolution). The electron scattering and the atomic vibrations are treated quantum mechanically. Dipolar scattering from long-wavelength optical vibrations is included. We present calculated atomically resolved vibrational-spectroscopic images of a polar crystalline material (hexagonal boron nitride). For such materials, dipole scattering from long optical vibrations can give rise to a strong background in the images, which has implications for the attainable spatial resolution. We show that an annular collection geometry can significantly reduce the dipole background, thereby reducing the electron dose required to observe atomic-scale contrast.

DOI: 10.1103/PhysRevB.96.224102

I. INTRODUCTION

It has recently become possible to use the high-energy electrons in a scanning transmission electron microscope (STEM) to perform vibrational spectroscopy of nanomaterials [1,2]. This technique can be used to map the vibrational properties of freestanding nanomaterials in a transmission geometry. To date, the technique has been applied to study the vibrational properties of ionic liquids [2], to detect the presence of molecular species [3,4], to study the vibrational excitations of beam-sensitive biological materials [5] (see also [6]), and to map excitations in dielectric materials [7,8]. Moreover, with the atomic-sized electron beams that can be generated in modern aberration-corrected STEMs, this advance opens the door for spatially resolved STEM vibrational spectroscopy at very high, perhaps even atomic, spatial resolution. In a recent work [9], we demonstrated experimentally a spatial resolution of the order of 1 nm. Such capabilities constitute a significant advance in the analysis of nanomaterials.

In a previous work [10], a theoretical analysis of vibrational-spectroscopic images of selected molecules showed that high, and even atomic, spatial resolution is allowed by the scattering physics. That analysis [10] included a realistic model of the dipole scattering from optical vibrational modes. In fact, the importance of dipole scattering in electron-vibrational spectroscopy was recognized decades ago in works such as those of Lucas *et al.* [11], who examined vibrational excitations in dielectric thin films, and Ibach and Mills [12] and Thiry *et al.* [13], who examined vibrational excitations at surfaces. It is mainly this scattering that has been utilized in the STEM experiments reported thus far [1–5,7,8]. If present, and it often is, dipole scattering typically produces a strong contribution; moreover, it is inherently long ranged, extending far beyond the atomic scale [14]. Hence a proper analysis of the dipole scattering is absolutely mandatory in the context of spatial resolution. This was also realized in the work of Rez [15], who examined the spatial resolution of vibrational scattering from molecules and also reached the conclusion that high spatial resolution should be possible.

The question of what spatial resolution might be achievable in vibrational mapping of extended specimens, particularly crystalline ones, is also of considerable interest [16–19]. For example, the resolution attained for a crystal foil may well dictate that achievable at interfaces and localized defects, which are also ultimately of great interest. In the case of acoustic-type modes, where long-ranged electric fields are absent, it is apparent from our understanding of high-angle annular dark-field imaging that atomic resolution should be achievable, as confirmed by recent works [17,18]. On the other hand, in the case of optical modes in polar crystals, long-ranged fields can build up with distance, causing dipole scattering which inadvertently affects the spatial resolution. Notwithstanding this, some recent works [17,18] omitted the dipole scattering, which could lead to erroneous conclusions when the optical modes are involved.

In this work, we outline a theory of advanced spatially resolved vibrational spectroscopy in the STEM, and we use it to analyze the feasibility of vibrational mapping of extended specimens at lattice resolution. The electron scattering and the atomic vibrations are treated quantum mechanically. Dipole scattering is included. The vibrational states are calculated using a Born–von Kármán model, as is necessary for a realistic account of the vibrational spectra. Later, we present calculated vibrational maps of (polar) hexagonal boron nitride, giving special attention to the spatial resolution and the signal strength afforded by the scattering physics. We show that vibrational maps of a polar material can be dominated by dipole scattering. We also show that dipole scattering can be reduced by using an off-axial collection geometry such as an annular collection aperture, thereby reducing the electron beam dose required to observe lattice contrast.

II. BACKGROUND

In STEM vibrational spectroscopy, a beam of accelerated electrons (∼100 keV) passes through a beam-defining aperture before being focused to a small crossover (typically, ∼0.1−1 nm) at the sample plane. The beam is scanned across the electron-transparent sample, which is typically up to

*christian.dwyer@asu.edu

several tens of nanometers thick. A collection aperture in the diffraction plane admits electrons that have been scattered through a certain angular range, allowing them to pass into the energy loss spectrometer. Vibrational spectra are acquired in synchronization with the scanning beam. A vibrational map of the sample is produced by plotting a particular spectral feature as a function of beam position to form an image.

We use Møller potentials to describe the inelastic scattering of high-energy electrons by a target (by which we mean an agglomerate of bonded atoms). Using the single-inelastic-scattering approximation, the wave function of an inelastically scattered electron in the diffraction plane can be written in the form

$$\begin{aligned}\psi_{q\nu}(\mathbf{k};\mathbf{x}_0) &\approx \int d^2\mathbf{x} \int_{-\infty}^{+\infty} dz\, iG(\mathbf{k},+\infty;\mathbf{x},z)(-i\sigma)V_{q\nu}(\mathbf{x},z) \\ &\quad\times \int d^2\mathbf{k}_0\, iG(\mathbf{x},z;\mathbf{k}_0,-\infty)\psi_0(\mathbf{k}_0;\mathbf{x}_0). \end{aligned} \tag{1}$$

Here z is the coordinate along the optic axis $\hat{z}$, bold symbols denote two-dimensional vectors transverse to $\hat{z}$, ψ_0 is the wave function of the incident beam focused at a position $\mathbf{x}_0$ on the target's entrance surface, the functions G are the propagators which account for the multiple elastic scattering before and after the single inelastic event, $V_{q\nu}$ is the Møller potential for exciting a certain quantum state of the target (here a vibrational mode $q\nu$), and $\sigma = 1/\hbar v$ is the interaction constant, where v is the incident electron's velocity. We have used a Fourier space representation for the incident wave function and mixed Fourier-coordinate representations for the propagators. This expression describes the wave function $\psi_{q\nu}$ as evolving from the plane of the beam-defining aperture before the sample (coordinatized by $\mathbf{k}_0$) to the diffraction plane after the sample (coordinatized by $\mathbf{k}$).

The vibrational signal for beam position $\mathbf{x}_0$ is obtained by integrating the appropriate inelastic intensity that falls inside the spectrometer collection aperture:

$$I(\mathbf{x}_0) = \sum_{q\nu}{}' \int_{\text{ap.}} d^2\mathbf{k}\, |\psi_{q\nu}(\mathbf{k};\mathbf{x}_0)|^2, \tag{2}$$

where the prime on the summation means to include only those vibrational modes having, say, energies within a chosen range. The intensity $I(\mathbf{x}_0)$ is a vibrational-spectroscopic image (or "vibrational map") of the target.

III. MODEL OF ATOMIC VIBRATIONS

We use a Born–von Kármán model based on the harmonic and adiabatic approximations [20]. This model is tailored for atomic vibrations in crystals, i.e., phonons, but it is also applicable to nonperiodic solids and molecules if a supercell with buffering layers of vacuum is used. The model also has the benefit that it is amenable to calculation using plane-wave density-functional codes.

For a crystal, the modes are labeled $q\nu$, where q is a wave vector in the first Brillouin zone of the primitive unit cell, and ν labels the branches which in number equal three times the number of atoms in the primitive unit cell. For a nonperiodic solid or molecule, the primitive unit cell and the supercell are the same, so that the Brillouin zone reduces to $q = 0$, and the modes are labeled solely by ν.

In the general case, the atoms are labeled by $l\kappa$, where l labels the primitive unit cell and κ labels the atom in the primitive cell. The displacement operator of nucleus $l\kappa$ can be written [20]

$$u(l\kappa) = \sum_{q\nu} [C^*_{q\nu}(l\kappa)a^*_{q\nu} + C_{q\nu}(l\kappa)a_{q\nu}], \tag{3}$$

where $a^*_{q\nu}$ and $a_{q\nu}$ are creation and annihilation operators for mode $q\nu$, respectively, and

$$C_{q\nu}(l\kappa) = \left(\frac{\hbar}{2Nm_\kappa\omega_{q\nu}}\right)^{1/2} e_{q\nu}(\kappa)e^{iq\cdot x_{l\kappa}}, \tag{4}$$

in which N is the number of primitive unit cells in the supercell, m_κ is an atomic mass, $\omega_{q\nu}$ and $e_{q\nu}(\kappa)$ are the angular frequency and (partial) eigenvector for mode $q\nu$, respectively, and $x_{l\kappa}$ is the equilibrium position of nucleus $l\kappa$. [We use the convention that the phase factor $e^{iq\cdot x_\kappa}$ containing the κth nucleus' position x_κ within the primitive unit cell is not contained in the eigenvectors $e_{q\nu}(\kappa)$ but appears explicitly in Eq. (4) as part of $e^{iq\cdot x_{l\kappa}}$.]

To calculate electron-vibrational scattering, we must reconcile the use of a Born–von Kármán supercell with the fact that the target is finite, and therefore not translationally invariant, along the direction parallel to the beam. We distinguish between the following two scenarios:

A *thin target* is small enough in the direction parallel to the beam that we can compute its modes using a Born–von Kármán supercell containing buffering layers of vacuum. This applies to extremely thin crystal foils, small nanoparticles, adsorbed molecules, etc. For thin targets in general, the modes are labeled $\mathbf{q}\nu$, where the parallel component $q_\parallel$ has been dropped and then for targets without translational invariance $\mathbf{q}$ is also dropped. All modes are included; for example, for a crystal foil the surface modes are included.

A *thick crystal foil* is too large in the parallel direction to be entirely contained within a supercell. Here we must be content with using a smaller Born–von Kármán supercell to calculate the bulk vibrational modes $q\nu$ in the conventional way. Then interpolation with respect to q can be performed and is equivalent to enlarging the bulk supercell. If the crystal thickness is an integral number of primitive unit cells, then the enlarged supercell can contain the entire foil (without vacuum), and the allowed $q_\parallel$ are commensurate with the periodic boundary condition across the thickness of the foil. Surface modes are neglected. Only the bulk modes are included.

IV. MØLLER POTENTIALS FOR VIBRATIONAL SCATTERING

Appendix A shows that the Møller potential for exciting mode $q\nu$ can be written in the form

$$V_{q\nu}(x) = \sum_{l\kappa} u_{q\nu}(l\kappa)\cdot\nabla_{l\kappa}\langle V(x)\rangle, \tag{5}$$

where $\langle V(x)\rangle$ is the thermally averaged interaction energy, $\nabla_{l\kappa}$ is a derivative with respect to the equilibrium position of

nucleus $l\kappa$, and

$$u_{q\nu}(l\kappa) = (\langle n_{q\nu}\rangle + 1)^{1/2} C^*_{q\nu}(l\kappa) = \left(\frac{\hbar(\langle n_{q\nu}\rangle + 1)}{2Nm_\kappa \omega_{q\nu}}\right)^{1/2} e^*_{q\nu}(\kappa) e^{-iq\cdot x_{l\kappa}}, \quad (6)$$

where $n_{q\nu}$ is the occupation number of mode $q\nu$. The quantity $u_{q\nu}(l\kappa)$ can be interpreted as the thermally averaged displacement of nucleus $l\kappa$ vibrating in the mode $q\nu$, with the caveat that this displacement is a complex quantity associated with a target transition $|n_{q\nu}\rangle \to |n_{q\nu}+1\rangle$. From Eq. (5), we see that $V_{q\nu}(x)$ is nothing but the first-order change in the thermally averaged potential caused by the nuclear displacements $\{u_{q\nu}(l\kappa)\}$.

We point out that we have *not* assumed a simple sum of electron-atom or electron-ion interactions. Hence the Møller potential in Eq. (5) is valid even in the case of strong covalent bonding of the atoms, for example. Notwithstanding this, the adiabatic approximation allows the Møller potentials to take the form of a sum over the atoms in the target, which facilitates their calculation.

We use multislice theory [21] to compute the dynamical elastic scattering embodied in the propagators G of Eq. (1). Multislice theory requires the *projected* Møller potentials, which are given by

$$V_{q\nu}(\mathbf{x}) = \int_{z_n}^{z_{n+1}} dz\, V_{q\nu}(\mathbf{x},z) e^{i\omega_{q\nu}z/v}, \quad (7)$$

where z_n and z_{n+1} define the bounding planes of the nth slice. The phase factor $e^{i\omega_{q\nu}z/v}$ accounts for the energy loss; that is, the parallel component of the beam electron's scattering vector is related to the energy loss via $k_\parallel = -\omega_{q\nu}/v$. In the case of a thin target, it is often convenient to set the limits of integration in Eq. (7) to $-\infty$ and $+\infty$, referred to as the *projection approximation*,

$$V_{q\nu}(\mathbf{x}) = \int_{-\infty}^{+\infty} dz\, V_{q\nu}(\mathbf{x},z) e^{i\omega_{q\nu}z/v} = \int \frac{d^2\mathbf{k}}{(2\pi)^2} V_{q\nu}(\mathbf{k}, -\omega_{q\nu}/v) e^{i\mathbf{k}\cdot\mathbf{x}}, \quad (8)$$

where the second equality follows from the Fourier projection theorem. The projection approximation neglects the curvature of the Ewald sphere. In practice, we use a combination of these two projection schemes: The sum over atoms in Eq. (5) means that atoms can be unambiguously assigned to a given slice, and then the contribution of these atoms is integrated over the full range of z values.

V. DIPOLE SCATTERING

Dipole scattering corresponds to the limit of small scattering vectors $k \to 0$. It is not possible to include these scattering vectors directly in a numerical calculation of the electron scattering. Hence the dipole contribution must be included "by hand." Dipole scattering can be considered to result from the vibrating target's macroscopic electric field, that is, the field obtained by averaging over a length scale that is much larger than the atoms but much smaller than the target overall. Macroscopic fields can extend well beyond the volume of the target and cause scattering in those regions. In the case of a crystal foil this includes the regions above and below the foil.

In vibrational mapping, dipole scattering gives rise to a background intensity. In the context of the present work, such a background can potentially mask a weaker high-spatial-resolution signal.

We first present the results obtained from the classical theory of electron scattering from a dielectric foil [11]. A succinct derivation will form part of a forthcoming publication [22]. A continuum dielectric description is valid for long optical modes. The theory predicts scattering from the bulk longitudinal modes and the surface modes of the dielectric foil. It is found that, for the thicknesses we are interested in, scattering from the surface modes dominates. Of the surface modes, the symmetry of the ungerade (uneven) modes leads to weak scattering, while that of the gerade (even) modes leads to the dominant scattering contribution. The intensity of scattering from a gerade mode labeled by wave vector $\mathbf{q}$ can be written in the form

$$\frac{dI_{\rm ger}}{d^2(\mathbf{q}/2\pi)} \approx \frac{1}{\Omega}\frac{e^2}{\hbar^2 v^2}\frac{\hbar}{2\mu\omega_{\mathbf{q}}}\frac{4|\mathbf{q}|e^{|\mathbf{q}|t}}{\sinh|\mathbf{q}|t}\left(\frac{Z_T^*}{\epsilon_\infty - \epsilon_{\mathbf{q}}}\right)^2 \times \left(\frac{4\pi}{|\mathbf{q}|^2 + \omega_{\mathbf{q}}^2/v^2}\right)^2, \quad (9)$$

where Z_T^* is the transverse effective charge and $\epsilon_{\mathbf{q}} = -\coth|\mathbf{q}|t/2$. In the limit $|\mathbf{q}|t \ll 1$, which we presume is valid for ultrathin foils, Eq. (9) simplifies, and we can perform the integration with respect to $\mathbf{q}$ for a circular aperture with a cutoff wave vector q_c:

$$I_{\rm ger} = \frac{t}{\Omega}\frac{e^2 Z_T^{*2}}{\hbar^2 v^2}\frac{\hbar}{2\mu\omega_T}\int^{q_c}\frac{d^2\mathbf{q}}{(2\pi)^2}\frac{(4\pi)^2|\mathbf{q}|^2}{\left(\mathbf{q}^2 + \omega_T^2/v^2\right)^2} \approx \frac{t}{\Omega}\frac{e^2 Z_T^{*2}}{\hbar^2 v^2}\frac{\hbar}{2\mu\omega_T}4\pi\ln\left(\frac{q_c^2}{\omega_T^2/v^2}\right), \quad (10)$$

where ω_T is the bulk transverse mode frequency and the approximation assumes $q_c \gg \omega_T/v$. The predictions of Eqs. (9) and (10) for dipole scattering from [0001] hexagonal boron nitride are shown in Fig. 1.

Having summarized the results from the classical theory, we now consider dipole scattering from a crystal foil using the Møller potential formalism. The modes of the crystal foil are labeled by $\mathbf{q}\nu$. Appendix B shows that the Møller potential for dipole scattering, for scattering vector $k = -\mathbf{q} - (\omega_{\mathbf{q}\nu}/v)\hat{z}$ with $\mathbf{q} \to \mathbf{0}$, can be written in the form

$$V_{\mathbf{q}\nu}(-\mathbf{q}, -\omega_{\mathbf{q}\nu}/v) = -ieN\frac{4\pi p_{\mathbf{q}\nu}\cdot[\mathbf{q} + (\omega_{\mathbf{q}\nu}/v)\hat{z}]}{\mathbf{q}^2 + \omega_{\mathbf{q}\nu}^2/v^2}, \quad (11)$$

where

$$p_{\mathbf{q}\nu} = \sum_\kappa u_{\mathbf{q}\nu}(\kappa)\cdot Z_\kappa^* \quad (\mathbf{q}\to\mathbf{0}). \quad (12)$$

$p_{\mathbf{q}\nu}$ is the dipole moment of the home primitive cell induced by the vibrational mode $\mathbf{q}\nu$ ($\mathbf{q}\to\mathbf{0}$). This dipole moment is composed of the mode displacements $u_{\mathbf{q}\nu}(\kappa)$ and the effective charge tensors Z_κ^*. For nonpolar materials $Z_\kappa^* = 0$, and there is no dipole scattering. For polar materials $p_{\mathbf{q}\nu} \neq 0$ for optical-type modes, and dipole scattering is allowed. From Eq. (11)

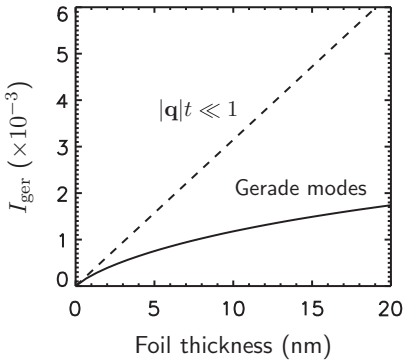

FIG. 1. Calculated dipole scattering probability of 60 keV electrons from the gerade modes of a dielectric foil [Eq. (9)]. The dielectric properties match [0001] hexagonal boron nitride, and the maximum thickness (20 nm) corresponds to 30 [0001]-oriented unit cells. A scattering cutoff of 0.7 mrad is assumed. The prediction assuming $|\mathbf{q}|t \ll 1$ [Eq. (10)] is also shown.

we see that the perpendicular and parallel components of $p_{\mathbf{q}\nu}$ have different selection rules: If the target is isotropic in the perpendicular directions, then only the longitudinal component $\hat{\mathbf{q}} \cdot \mathbf{p}_{\mathbf{q}\nu}$ contributes. For the parallel component $p_{\|\mathbf{q}\nu}$ there is no such restriction, although its contribution is small owing to the smallness of $\omega_{\mathbf{q}\nu}/v$.

Let us assume a polar crystal foil that is isotropic in the perpendicular directions and consider the in-plane LO-type modes. Using Eq. (11) the probability that an incident electron in a plane wave state undergoes dipole scattering is given by

$$I_\nu = \frac{1}{V_\perp}\left(\frac{1}{\hbar v}\right)^2 \int^{q_c} \frac{d^2\mathbf{q}}{(2\pi)^2} |V_{\mathbf{q}\nu}(-\mathbf{q}, -\omega_{\mathbf{q}\nu}/v)|^2 = \frac{e^2 N}{\hbar^2 v^2 \Omega_\perp} \int^{q_c} \frac{d^2\mathbf{q}}{(2\pi)^2} \frac{(4\pi)^2 |\mathbf{p}_{\mathbf{q}\nu}|^2 \mathbf{q}^2}{\left(\mathbf{q}^2 + \omega_{\mathbf{q}\nu}^2/v^2\right)^2}, \tag{13}$$

where q_c is a cutoff wave vector. The dipole squared can be written

$$|p_{q\nu}|^2 = \frac{\hbar(\langle n_{q\nu}\rangle + 1)}{2N\omega_{q\nu}} \left| \sum_\kappa \frac{e^*_{q\nu}(\kappa)}{m_\kappa^{1/2}} \cdot Z^*_\kappa e^{-iq\cdot x_\kappa} \right|^2, \tag{14}$$

so in Eq. (13) the factor of N cancels. Equation (13) predicts the dipole scattering for a general polarization $\mathbf{p}_{\mathbf{q}\nu}$, including surface modes.

Because the Møller potential for dipole scattering is slowly varying in coordinate space, the result for a plane wave is also applicable to a focused electron beam, provided that the beam wave function is significantly narrower than the delocalization distance (which we assume to be the case). Moreover, the small scattering angles imply that the dipole scattering closely follows any larger-angle scattering, such as elastic scattering.

We can show that in the limit of ultrathin targets, Eq. (13) agrees with the classical result (10). To this end, we further assume a crystal structure with a primitive unit cell containing $2s$ atoms, s of which are cations of the same species, having effective charge $+Z^*$ and mass m_+, and the other s being anions of the same species, having charge $-Z^*$ and mass m_-. Common examples include LiF, BN, SiC, and GaAs. When $q \to 0$, the optical mode displacement eigenvectors satisfy $m_+^{1/2} e(+) = -m_-^{1/2} e(-)$, and it can be shown that

$$|p_{q\nu}|^2 = \frac{\hbar(\langle n_{q\nu}\rangle + 1)}{2N\omega_{q\nu}} \frac{Z^{*2}}{\mu}, \tag{15}$$

where the effective mass is defined by $\mu^{-1} = \sum_\kappa m_\kappa^{-1}$. We assume $\langle n_{\mathbf{q}\nu}\rangle \approx 0$ for optical modes. If we neglect any variation of $|\mathbf{p}_{\mathbf{q}\nu}|^2$ and $\omega_{\mathbf{q}\nu}$ with respect to $\mathbf{q}$, which is valid for ultrathin targets, then the integral in Eq. (13) can be performed, and we obtain, finally,

$$I_\nu \approx \frac{t}{\Omega} \frac{e^2 Z_T^{*2}}{\hbar^2 v^2} \frac{\hbar}{2\mu\omega_\nu} 4\pi \ln\left(\frac{q_c^2}{\omega_\nu^2/v^2}\right), \tag{16}$$

which is the same as the classical result (10).

An analogous calculation can be performed for dipole scattering from out-of-plane transverse or longitudinal optical-type modes. The result, again valid for ultrathin targets, is

$$I_\nu \approx \frac{t}{\Omega} \frac{e^2 Z_L^{*2}}{\hbar^2 v^2} \frac{\hbar(\langle n_\nu\rangle + 1)}{2\mu\omega_\nu} 4\pi,. \tag{17}$$

where Z_L^* is the longitudinal effective charge. Note that here the intensity rapidly converges with scattering angle, so unlike the result for in-plane modes, there is no dependence on q_c for $q_c \gg \omega_\nu/v$. For typical parameters, the contribution from out-of-plane modes tends to be at least an order of magnitude smaller than that from in-plane modes.

Equations (16) and (17) are useful for estimating the dipole scattering from ultrathin crystals. For thicker crystals we require either the full classical result (9) or the quantum result (13).

In the context of vibrational mapping, the question of the appropriate cutoff q_c requires consideration since, on the one hand, q_c is assumed to be small (e.g., for a continuum dielectric description to hold), while, on the other hand, the geometry used for mapping experiments generally admits much larger q's. A method for choosing q_c is described in the next section.

VI. NUMERICAL RESULTS

Below we consider calculated spatially resolved vibrational maps of [0001] hexagonal boron nitride. We assume an aberration-free 60 keV beam with a 30-mrad convergence semiangle (which gives a probe size of 0.9 Å FWHM). The elastic and inelastic (vibrational) electron scattering was calculated using a multislice approach combined with the Møller potential formalism, as embodied in Eqs. (1), (2), (7), and (8). A supercell comprising 16×16 h-BN unit cells was used for the electron scattering calculations.

We used density functional theory and the finite-displacement method to calculate the vibrational modes of h-BN. The finite-displacement method allows us to incorporate the changes in electronic bonding charge associated with vibrational modes (which, in the limit of long wavelengths, is described by the effective charges). We treated single-layer BN as a thin target (see Sec. III), and we used a $4 \times 4 \times 1$ supercell in which the atomic layers are separated by 2.5 nm of vacuum. We treated the thicker BN samples as thick crystal foils (see Sec. III), and we calculated their bulk modes using a $4 \times 4 \times 1$ supercell. The calculated phonon dispersion of single-layer BN is shown in Fig. 2. Also shown in Fig. 2

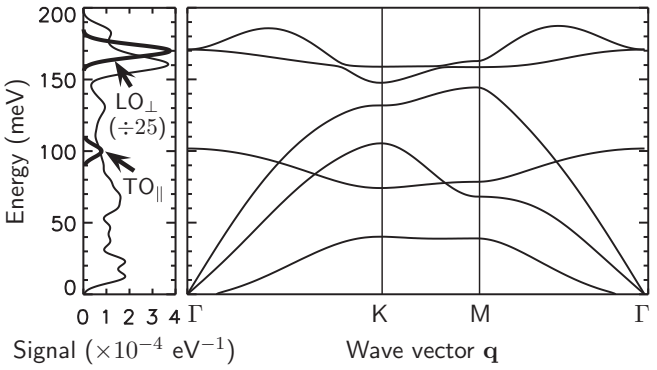

FIG. 2. Calculated position-averaged vibrational energy loss spectra and phonon dispersions of single-layer h-BN. The spectrum also shows the dipole contributions from in-plane LO modes at 170 meV (whose intensity is 25 times larger than indicated) and out-of-plane optical modes at 102 meV. The spectrum assumes a resolution of 10 meV.

is the position-averaged vibrational spectrum, for which the collection angle matches the convergence angle. The lightness of B and N atoms and the strong in-plane electronic bonding cause hexagonal boron nitride to exhibit high-energy optical phonon modes (Fig. 2) that lie well within the spectral range of new-generation STEMs. The vibrational-spectroscopic images presented assume an energy window of 150–200 meV (1200–1600 cm^{-1}), which includes contributions mainly from the highest-energy optical phonons.

We used density functional perturbation theory to calculate the Born effective charges for h-BN. We obtained $Z^*_{\mathrm{B}\perp} = -Z^*_{\mathrm{N}\perp} = 2.70e$, in good agreement with others [23]. The effective charges in h-BN give rise to strong dipole scattering. Following our previous discussion, the dipole scattering forms a background in the vibrational map which mimics the elastic signal. The dipole contribution is given by the probability of elastic scattering multiplied by the probability that a plane wave undergoes dipole scattering. We used the dipole scattering probability for the gerade modes plotted in Fig. 1, where the 0.7-mrad scattering cutoff assumed there corresponds to vibrational modes with wavelengths larger than the 16×16 supercell used for the results in Fig. 3. Hence in Fig. 3 the dipole contribution consists of scattering from modes with wavelengths too large to be contained within the supercell.

Figure 3 shows the calculated vibrational-spectroscopic images of [0001] h-BN. Images are shown for thicknesses of 1 atomic layer, 5 unit cells (3.3 nm), and 30 unit cells (20 nm) and for collection semiangles $\beta = 10$, 30, and 50 mrad (i.e., smaller than, equal to, and larger than the convergence semiangle). For $\beta = 10$ mrad, we see that for the thinner samples the intensity maxima do not necessarily correspond to the atomic positions. Such behavior, which is often observed when the collection angle is smaller than the convergence angle, makes it difficult to interpret the vibrational images directly in terms of the atomic structure. Moreover, the small collection angle omits a significant proportion of the scattering, giving rise to lower intensities, as shown by the line traces in Fig. 3. Increasing the collection semiangle to 30 mrad and then further to 50 mrad greatly improves the interpretability of the vibrational maps; that is, intensity maxima correspond to the atomic sites, as well as increasing the overall intensity.

The line traces in Fig. 3 also show the dipole scattering contributions. For single-layer BN, we see that the dipole background comprises the major contribution, and it results in images with very low contrast. In this case the dipole background is flat since there is negligible elastic scattering. For the thickest sample, the dipole scattering comprises only about 1/3 of the vibrational signal, although it can still lead to a substantially reduced image contrast, e.g., for $\beta = 50$ mrad.

VII. DISCUSSION

An important consequence of a strong dipole background is that more incident electrons are needed to observe the atomic-scale contrast in an experiment. To estimate the minimum number of incident electrons required, we assume an ideal scenario where the only noise source is the shot noise. We let the level of shot noise correspond to the mean number of scattered electrons in the vibrational map. This noise level is $\sqrt{N_e \langle I \rangle}$, where N_e is the mean number of incident electrons per pixel (the pixel size being appropriately matched to the atomic-scale contrast) and $\langle I \rangle$ is the mean intensity. It follows that observation of atomic-scale contrast requires a dose $N_e \gtrsim \langle I \rangle / (\Delta I)^2$, where ΔI is the magnitude of the atomic-scale intensity variations. This required dose increases with decreasing contrast, as expected.

It has been suggested in several works [9,10,17,19] that an annular collection geometry with an inner angle slightly larger than the convergence angle could be used to reject the majority of the low-angle dipole scattering and thereby improve the atomic-scale contrast. In terms of the electron dose N_e, such a geometry essentially corresponds to reducing $\langle I \rangle$ while maintaining or increasing ΔI, thereby lowering N_e. An annular geometry may have other important benefits too, such as partially alleviating the experimental challenge of energy resolution versus collection angle and significantly reducing the strong elastic peak in the energy-loss spectrum (potentially a significant source of noise in vibrational spectroscopy).

Figure 4 shows calculated vibrational-spectroscopic images and line traces for an annular collection range of 35–50 mrad. These results should be compared with the $\beta = 50$ mrad cases in Fig. 3 (which have the same outer angle). In Fig. 4 it is seen that an annular geometry results in directly interpretable images in the sense described above. Importantly, the image contrast is also dramatically improved, leading to lower electron beam doses for atomic resolution. For single-layer BN, the annular geometry reduces N_e from 1×10^5 to 2×10^4. For a thickness of 30 unit cells, N_e is reduced from 1×10^4 to 4×10^3. Note that our simple model for calculating N_e assumes a "direct" observation of atomic contrast in the vibrational-spectroscopic images. In crystalline samples, averaging techniques can provide a means of reducing N_e by an order of magnitude or more. On the other hand, experiments contain noise other than the shot noise in our simple model, which will again increase the required dose.

Before concluding, we should distinguish between the present results for crystals and our previous results on isolated molecules. In previous work [10], we showed that, even

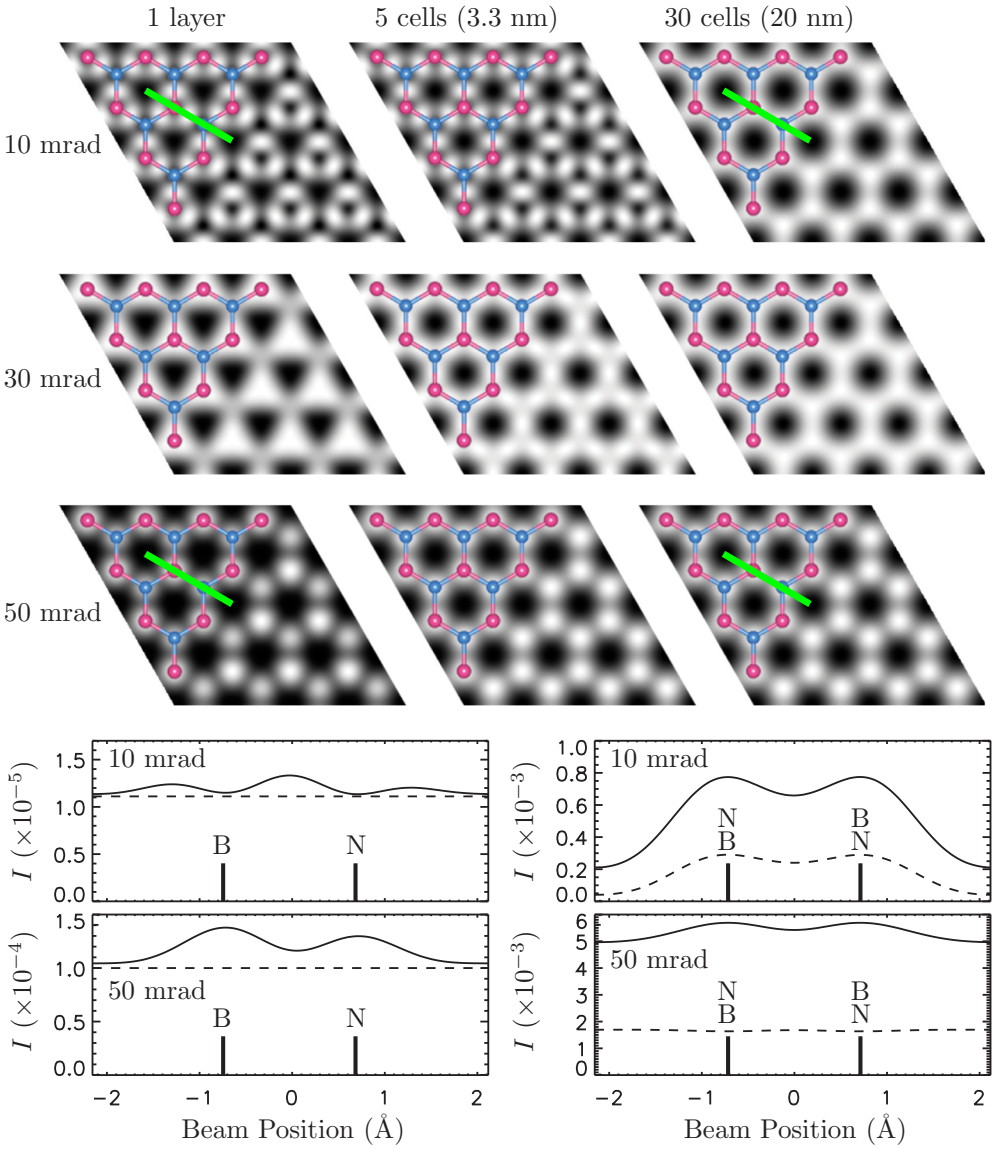

FIG. 3. Calculated vibrational-spectroscopic images and line traces of *h*-BN. For the images, the sample thickness and collection semiangle are indicated; atomic models of BN are overlaid (for one layer, B is red and N is blue); gray scales are linear, with the minimum and maximum intensities represented as black and white. For the line traces, the beam paths are indicated by green lines on the images; I is the scattering probability (solid lines), and the dipole scattering contribution is shown separately (dashed lines). A beam energy of 60 keV, convergence semiangle of 30 mrad, and energy window of 150–200 meV apply throughout.

for a molecule that is strongly polar, the dipole scattering does not necessarily mask the atomic contrast. This is in contrast to results in Fig. 3. The different conclusions can be understood quite simply: In crystals, the dipole fields of a very large number of unit cells can add up to produce a strong macroscopic field at a given position, but for an isolated molecule the dipole field originates only from that single molecule, so it remains comparatively weak.

VIII. CONCLUSION

In summary, we have presented a quantum-mechanical theory of advanced spatially resolved vibrational electron energy loss spectroscopy in the STEM. Numerical calculations of vibrational maps for BN, a polar material, have shown that the dipole scattering, which is manifest as a background in the vibrational maps, can lead to substantially reduced atomic-scale contrast. We have shown that an annular collection geometry is effective in reducing the dipole background in the case of BN, and this conclusion should extend to other polar materials. This and the aforementioned benefits of an annular geometry appear to provide a viable route for pursuing high-resolution STEM vibrational electron energy loss spectroscopy in the future.

APPENDIX A: MØLLER POTENTIALS FOR VIBRATIONAL EXCITATIONS

The Møller potentials will be derived by considering the thermal average of the scattered electron intensity. First,

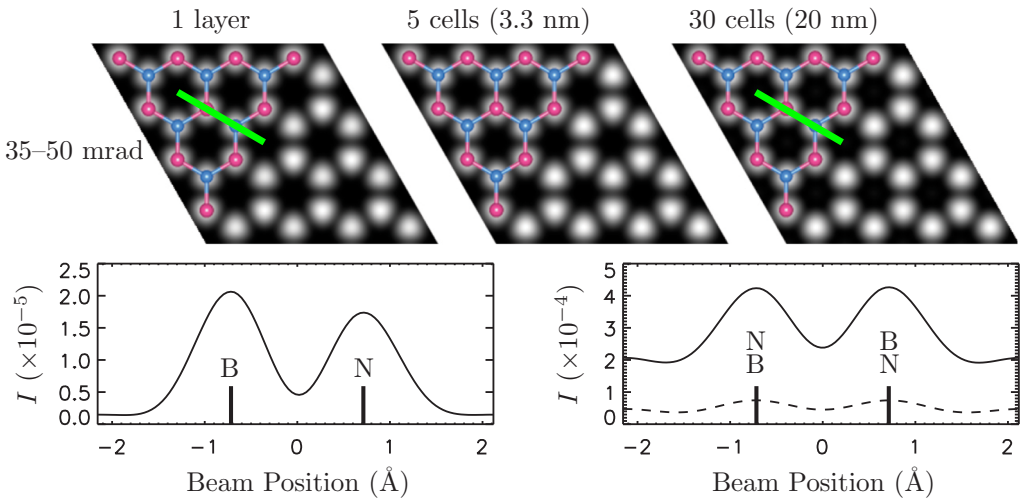

FIG. 4. Calculated vibrational-spectroscopic images and line traces of h-BN for an annular collection aperture spanning 35–50 mrad. All other parameters match Fig. 3.

we consider the instantaneous Coulomb interaction energy between the beam electron and the target. Adopting the adiabatic (Born-Oppenheimer) approximation, the interaction energy is a function of the beam electron's coordinate, denoted by x, and the instantaneous positions of the nuclei. The nuclear coordinates are $x_{l\kappa}+u(l\kappa)$, where $x_{l\kappa}$ is the equilibrium position and $u(l\kappa)$ is the displacement from equilibrium. The dependence on $x_{l\kappa}$ will not be written explicitly, so that $V(x,u)$ will denote the interaction with the nuclei displaced, while $V(x)$ will denote the interaction without displacements. Hence we write the instantaneous Coulomb interaction as a Taylor expansion with respect to the nuclear displacements,

$$V(x,u)=e^{\sum_{l\kappa}u(l\kappa)\cdot\nabla_{l\kappa}}V(x), \tag{A1}$$

where the gradient $\nabla_{l\kappa}$ is with respect to the equilibrium position $x_{l\kappa}$ of nucleus $l\kappa$. We introduce the shorthand notation

$$u\cdot\nabla\equiv\sum_{l\kappa}u(l\kappa)\cdot\nabla_{l\kappa}=\sum_{q\nu}[D^{*}_{q\nu}a^{*}_{q\nu}+D_{q\nu}a_{q\nu}], \tag{A2}$$

where $D_{q\nu}$ is the displacement operator for mode $q\nu$, defined by

$$D_{q\nu}=\sum_{l\kappa}C_{q\nu}(l\kappa)\cdot\nabla_{l\kappa}, \tag{A3}$$

where $C_{q\nu}(l\kappa)$ is given by Eq. (4). The instantaneous interaction becomes

$$V(x,u)=e^{u\cdot\nabla}V(x). \tag{A4}$$

To derive the Møller potentials we adopt a kinematical approximation and consider the thermal average of the intensity of electrons scattered by a wave vector k. Note that this does not mean that the final theory will be kinematical. Rather, the kinematic approximation is used here as a tool to derive the Møller potentials. This method of deriving the Møller potentials for vibrational scattering is based on the work of Anstis [24], who used an Einstein model in a semiclassical description of thermal-diffuse scattering. Here the method is applied using a quantum-mechanical Born–von Kármán model.

The thermally averaged kinematical intensity is

$$\langle I(k,u)\rangle\propto\langle|V(k,u)|^{2}\rangle, \tag{A5}$$

where $V(k,u)$ is the Fourier transform of $V(x,u)$ with respect to the electron coordinate x and the angular brackets denote the thermal average over the nuclear displacements $u_{l\kappa}$. We will see that this thermal average can written as a sum of intensities,

$$\langle I(k,u)\rangle\propto|V_0(k)|^{2}+|V_1(k)|^{2}+|V_2(k)|^{2}+\cdots, \tag{A6}$$

where $|V_0|^2$ is (proportional to) the elastic intensity and $|V_1(k)|^2,|V_2(k)|^2,\ldots$ are (proportional to) the inelastic intensities associated vibrational excitations. $V_1(k),V_2(k),\ldots$ will turn out to be the Møller potentials.

Write the thermally averaged interaction in the form

$$\begin{aligned}\langle V^{*}(k,u)V(k,u)\rangle&=\langle V^{*}(k)e^{u^{*}\cdot\overleftarrow{\nabla}}e^{u\cdot\overrightarrow{\nabla}}V(k)\rangle\\&=V^{*}(k)\langle e^{u^{*}\cdot\overleftarrow{\nabla}}e^{u\cdot\overrightarrow{\nabla}}\rangle V(k),\end{aligned} \tag{A7}$$

where the arrows indicate whether the derivative acts to the left or right and the second equality follows because $V(k)$ does not depend on u. We are left to evaluate

$$\begin{aligned}\langle e^{u^{*}\cdot\overleftarrow{\nabla}}e^{u\cdot\overrightarrow{\nabla}}\rangle&=\langle e^{u\cdot\overleftarrow{\nabla}}e^{u\cdot\overrightarrow{\nabla}}\rangle=\langle e^{u\cdot(\overleftarrow{\nabla}+\overrightarrow{\nabla})}\rangle=e^{\frac{1}{2}\langle[u\cdot(\overleftarrow{\nabla}+\overrightarrow{\nabla})]^{2}\rangle}\\&=e^{\frac{1}{2}\langle[u\cdot\overleftarrow{\nabla}]^{2}\rangle}e^{\langle[u\cdot\overleftarrow{\nabla}][u\cdot\overrightarrow{\nabla}]\rangle}e^{\frac{1}{2}\langle[u\cdot\overrightarrow{\nabla}]^{2}\rangle},\end{aligned} \tag{A8}$$

where the first equality follows from the displacement operators being Hermitian, the second follows because the sums of displacement operators in the exponents commute, and the third and fourth equalities follow from a straightforward generalization of Eq. (7.2.22) of Ref. [20]. The exponents have the forms

$$\frac{1}{2}\langle[u\cdot\overrightarrow{\nabla}]^{2}\rangle=\sum_{q\nu}|\overrightarrow{D}_{q\nu}|^{2}\left(\langle n_{q\nu}\rangle+\frac{1}{2}\right) \tag{A9}$$

and

$$\begin{aligned}\langle[u\cdot\overleftarrow{\nabla}][u\cdot\overrightarrow{\nabla}]\rangle=\sum_{q\nu}[&\overleftarrow{D}_{q\nu}\overrightarrow{D}^{*}_{q\nu}(\langle n_{q\nu}\rangle+1)\\&+\overleftarrow{D}^{*}_{q\nu}\overrightarrow{D}_{q\nu}\langle n_{q\nu}\rangle],\end{aligned} \tag{A10}$$

where $\langle n_{q\nu}\rangle$ is the average mode occupation.

The exponential factors on the left and right of the last line of Eq. (A8) are identified as Debye-Waller factors, whose effect is to produce the thermally averaged interaction on the left and right:

$$\langle V^*(k,u)V(k,u)\rangle = \langle V^*(k,u)\rangle e^{\langle[u\cdot\overleftarrow{\nabla}][u\cdot\overrightarrow{\nabla}]\rangle}\langle V(k,u)\rangle. \quad \text{(A11)}$$

The remaining exponential factor on the right entails all possible vibrational excitations. It can be written in the form

$$e^{\langle[u\cdot\overleftarrow{\nabla}][u\cdot\overrightarrow{\nabla}]\rangle} = \prod_{q\nu} e^{\overleftarrow{D}_{q\nu}\overrightarrow{D}^*_{q\nu}(\langle n_{q\nu}\rangle+1)} e^{\overleftarrow{D}^*_{q\nu}\overrightarrow{D}_{q\nu}\langle n_{q\nu}\rangle}. \quad \text{(A12)}$$

The exponential containing $\langle n_{q\nu}\rangle + 1$ corresponds to the creation of vibrational quanta, and that containing $\langle n_{q\nu}\rangle$ corresponds to their destruction. Taylor expanding these exponentials, we obtain individual terms of the form

$$\prod_{q\nu}\frac{1}{p_{q\nu}!}[\overleftarrow{D}_{q\nu}\overrightarrow{D}^*_{q\nu}(\langle n_{q\nu}\rangle+1)]^{p_{q\nu}} \times\frac{1}{q_{q\nu}!}(\overleftarrow{D}^*_{q\nu}\overrightarrow{D}_{q\nu}\langle n_{q\nu}\rangle)^{q_{q\nu}}, \quad \text{(A13)}$$

where $p_{q\nu}\geqslant 0$ and $q_{q\nu}\geqslant 0$ are integers, which should be interpreted as the number of $q\nu$ quanta created and destroyed, respectively.

With this last expression, we have accomplished our present goal of writing the thermally averaged scattered intensity in the form

$$\langle I(k,u)\rangle \propto \sum_{\{p_{q\nu}\}}\sum_{\{q_{q\nu}\}}|V_{\{p_{q\nu}\}\{q_{q\nu}\}}(k)|^2, \quad \text{(A14)}$$

where $\{p_{q\nu}\} = \{p_{(q\nu)_1}, p_{(q\nu)_2},\dots\}$ and $\{q_{q\nu}\} = \{q_{(q\nu)_1}, q_{(q\nu)_2},\dots\}$, so that the sum is over all of the possible ways that the vibrational quanta $(q\nu)_1, (q\nu)_2,\dots$ can be created and/or destroyed. Explicitly, $V_{\{p_{q\nu}\}\{q_{q\nu}\}}$ is given by

$$V_{\{p_{q\nu}\}\{q_{q\nu}\}}(k) = \prod_{q\nu}\sqrt{\frac{(\langle n_{q\nu}\rangle+1)^{p_{q\nu}}\langle n_{q\nu}\rangle^{q_{q\nu}}}{p_{q\nu}!q_{q\nu}!}} \times D^{*p_{q\nu}}_{q\nu}D^{q_{q\nu}}_{q\nu}\langle V(k,u)\rangle. \quad \text{(A15)}$$

As a sanity check, elastic scattering corresponds to setting all p's and q's equal to zero, which gives the thermally averaged Coulomb interaction $\langle V(k,u)\rangle$, as expected. There are, in fact, an infinite number of other scattering terms in which the numbers of vibrational quanta are ultimately unchanged and so which constitute part of the elastic scattering. These are terms for which the p's exactly match the q's, so that quanta are created and destroyed in exactly equal numbers. This is the virtual inelastic scattering, which is needed to conserve the total number of electrons that are scattered elastically and inelastically. However, the potentials for virtual inelastic scattering are at least second order in the (small) atomic displacements, and therefore the effects are small, and they will be neglected.

In contrast, proper inelastic scattering corresponds to at least one of the p's being different from the q's. In this work, we assume a first-order creation event, i.e., $\{p_{q\nu}\} = \{0\cdots010\cdots0\}$ and $\{q_{q\nu}\} = \{0\cdots0\}$. We denote a Møller potential for such scattering by $V_{q\nu}(k)$, where $q\nu$ is the mode of the single quantum created. Explicitly,

$$V_{q\nu}(k) = (\langle n_{q\nu}\rangle+1)^{1/2}D^*_{q\nu}\langle V(k,u)\rangle, \quad \text{(A16)}$$

where the complex conjugate displacement operator $D^*_{q\nu}$ signifies the creation of one quantum of mode $q\nu$. Using the definitions above, $V_{q\nu}(k)$ can also be written in the form

$$V_{q\nu}(k) = \sum_{l\kappa} u_{q\nu}(l\kappa)\cdot\nabla_{l\kappa}\langle V(k,u)\rangle, \quad \text{(A17)}$$

where

$$u_{q\nu}(l\kappa) = (\langle n_{q\nu}\rangle+1)^{1/2}C^*_{q\nu}(l\kappa) = \left(\frac{\hbar(\langle n_{q\nu}\rangle+1)}{2Nm_\kappa\omega_{q\nu}}\right)^{1/2} e^*_{q\nu}(\kappa)e^{-iq\cdot x_{l\kappa}}. \quad \text{(A18)}$$

An inverse Fourier transform gives the Møller potential in coordinate space (5). Elsewhere in this article we write $\langle V(k)\rangle$ instead of $\langle V(k,u)\rangle$.

APPENDIX B: MØLLER POTENTIALS FOR DIPOLAR SCATTERING

Here we assume a crystal foil with surfaces. In Fourier space, the thermally averaged Coulomb interaction is

$$\langle V(k)\rangle = -e\frac{4\pi}{k^2}\langle\rho(k)\rangle, \quad \text{(B1)}$$

where $\langle\rho(k)\rangle$ is the Fourier transform of the target's thermally averaged charge density. We write the charge density in the form

$$\langle\rho(k)\rangle = \sum_l\langle\rho_l(k)\rangle, \quad \text{(B2)}$$

where we have assigned charge density to each of the primitive cells (which can be done unambiguously using a Wannier basis for the electrons [25]). Moreover, the crystal periodicity in the perpendicular directions implies

$$\nabla_{l'\kappa}\langle\rho_l(k)\rangle = e^{-i\mathbf{k}\cdot\mathbf{x}_l}\nabla_{(l'-l)\kappa}\langle\rho_0(k)\rangle, \quad \text{(B3)}$$

where ρ_0 is the charge density of the home primitive cell $l = 0$. Using this expression, we can obtain the following form of the Møller potential involving ρ_0:

$$V_{\mathbf{q}\nu}(k) = -e\frac{4\pi}{k^2}N\sum_{\mathbf{g}}\delta_{\mathbf{k}+\mathbf{q}-\mathbf{g}} \times\sum_{l\kappa}e^{+i\mathbf{k}\cdot\mathbf{x}_l}u_{\mathbf{q}\nu}(\kappa)\cdot\nabla_{l\kappa}\langle\rho_0(k)\rangle. \quad \text{(B4)}$$

Dipole scattering corresponds to the limit $\mathbf{k}\to\mathbf{0}$, $k_\parallel = -\omega_{q\nu}/v$. Only the $\mathbf{g} = \mathbf{0}$ term contributes. We further analyze the right-hand side of Eq. (B4) in the limit $k\to 0$. In the definition of the Fourier transform $\langle\rho_0(k)\rangle$, Taylor expanding the exponential $e^{-ik\cdot x}$, the term of zeroth order in k vanishes on account of charge neutrality, so to first order in k, we obtain

$$\sum_l e^{+ik\cdot x_l}\nabla_{l\kappa}\langle\rho_0(k)\rangle = \sum_l e^{+ik\cdot x_l}\nabla_{l\kappa}\int d^3x\,\langle\rho_0(x)\rangle x\cdot(-ik). \quad \text{(B5)}$$

When $k \to 0$, the right-hand side involves the change in the home primitive cell's dipole caused by a rigid displacement of the sublattice κ. Hence we can identify the effective charge tensor

$$Z^*_\kappa = \sum_l e^{+ik\cdot x_l} \nabla_{l\kappa} \int d^3x \, \langle \rho_0(x) \rangle x, \quad k \to 0. \tag{B6}$$

The effective charges given by this expression are easily shown to satisfy the acoustic sum rule $\sum_\kappa Z^*_\kappa = 0$. Finally, let us define

$$p_{q\nu} = \sum_\kappa u_{q\nu}(\kappa) \cdot Z^*_\kappa, \quad q \to 0, \tag{B7}$$

which is the dipole moment of the home primitive cell induced by the vibrational mode $q\nu$ ($q \to 0$).

Replacing $q\nu \to \mathbf{q}\nu$ in these definitions and using them in Eq. (B4), we find that the Møller potential for dipole scattering from a crystal foil with surfaces can be written in the form

$$V_{\mathbf{q}\nu}(-\mathbf{q}, -\omega_{\mathbf{q}\nu}/v) = -ieN \frac{4\pi p_{\mathbf{q}\nu} \cdot [\mathbf{q} + (\omega_{\mathbf{q}\nu}/v)\hat{z}]}{\mathbf{q}^2 + \omega^2_{\mathbf{q}\nu}/v^2}. \tag{B8}$$

For a target without periodicity along the perpendicular directions, we should replace $\mathbf{q}\nu \to \nu$ and drop the correspondence between the mode ν and the vector $\mathbf{q}$.

[1] O. L. Krivanek, T. C. Lovejoy, N. Dellby, T. Aoki, R. W. Carpenter, P. Rez, E. Soignard, J. Zhu, P. E. Batson, M. Lagos, R. F. Egerton, and P. A. Crozier, Nature (London) **514**, 209 (2014).

[2] T. Miyata, M. Fukuyama, A. Hibara, E. Okunishi, M. Mukai, and T. Mizoguchi, Microscopy **63**, 377 (2014).

[3] P. A. Crozier, K. March, and Q. Liu, Ultramicroscopy **169**, 30 (2016).

[4] P. A. Crozier, Ultramicroscopy **180**, 104 (2017).

[5] P. Rez, T. Aoki, K. March, D. Gur, O. L. Krivanek, N. Dellby, T. C. Lovejoy, S. G. Wolf, and H. Cohen, Nat. Commun. **7**, 10945 (2016).

[6] G. Radtke, D. Taverna, M. Lazzeri, and E. Balan, Phys. Rev. Lett. **119**, 027402 (2017).

[7] M. J. Lagos, A. Trügler, U. Hohenester, and P. E. Batson, Nature (London) **543**, 529 (2017).

[8] A. A. Govyadinov, A. Konecna, A. Chuvilin, S. Velez, I. Dolado, A. Y. Nikitin, S. Lopatin, F. Casanova, L. E. Hueso, J. Aizpurua, and R. Hillenbrand, Nat. Commun. **8**, 95 (2017).

[9] C. Dwyer, T. Aoki, P. Rez, S. L. Y. Chang, T. C. Lovejoy, and O. L. Krivanek, Phys. Rev. Lett. **117**, 256101 (2016).

[10] C. Dwyer, Phys. Rev. B **89**, 054103 (2014).

[11] A. A. Lucas, E. Kartheuser, and R. G. Badro, Phys. Rev. B **2**, 2488 (1970).

[12] H. Ibach and D. L. Mills, *Electron Energy Loss Spectroscopy and Surface Vibrations* (Academic, London, 1982).

[13] P. A. Thiry, M. Liehr, J. J. Pireaux, and R. Caudano, Phys. Scr. **35**, 368 (1987).

[14] R. F. Egerton, Microsc. Microanal. **20**, 658 (2014).

[15] P. Rez, Microsc. Microanal. **20**, 671 (2014).

[16] A. Howie, Ultramicroscopy **151**, 116 (2015).

[17] N. R. Lugg, B. D. Forbes, S. D. Findlay, and L. J. Allen, Phys. Rev. B **91**, 144108 (2015).

[18] B. D. Forbes and L. J. Allen, Phys. Rev. B **94**, 014110 (2016).

[19] A. Howie, Ultramicroscopy **180**, 52 (2017).

[20] A. A. Maradudin, E. W. Montroll, and G. H. Weiss, *Theory of Lattice Dynamics in the Harmonic Approximation*, 2nd ed. (Academic, London, 1971).

[21] E. J. Kirkland, *Advanced Computing in Electron Microscopy*, 2nd ed. (Springer, New York, 2010).

[22] D. D. Kordahl and C. Dwyer (unpublished).

[23] K. H. Michel and B. Verberck, Phys. Rev. B **83**, 115328 (2011).

[24] G. R. Anstis, Acta Crystallogr., Sect. A **52**, 450 (1996).

[25] N. Marzari, A. A. Mostofi, J. R. Yates, I. Souza, and D. Vanderbilt, Rev. Mod. Phys. **84**, 1419 (2012).